Research Square

Preprints are preliminary reports that have not undergone peer review.
They should not be considered conclusive, used to inform clinical practice,
or referenced by the media as validated information.

The Uruana de Minas geomagnetic anomaly remains aligned with mapped geological structures across four decades

Lucas Giovani Ribeiro

coin26@mail.com

Independent Researcher

Marcos André Simonssini

Independent Researcher

Research Article

Keywords: aeromagnetic data, magnetic-gradient anomaly, structural geology, Hessian eigenframe, multiepoch persistence, scalar–triaxial magnetometry

Posted Date: November 9th, 2026

DOI: https://doi.org/10.21203/rs.3.rs-11275531/v1

License: This work is licensed under a Creative Commons Attribution 4.0 International License.
Read Full License

Additional Declarations: No competing interests reported.

Abstract

A persistent crustal boundary may preserve its geometry across magnetic surveys that do not reproduce amplitude. We characterize the partial magnetic-gradient envelope at Uruana de Minas, Brazil, using archives from 1971–1972, 2008 and 2011. The 2011 raw-field gradient reversal supplies the geographic anchor. Historical and 2008 reconstructions recover opposed directional-derivative walls in a fixed 7–9 km annulus, with midpoints near Uruana. A historical bilinear model predicts withheld flight lines with a pooled error of 3.34 nT, compared with 5.00 nT for a plane. Magnetic and independently mapped geological orientation domains reconstruct one another with a worst held-out error of 2.287°, ranking first among 28 supported centers. The 1971-to-2008 eigenframe rotates by only 3.328° despite curvature-spectrum change. Raw-to-corrected 2008 Hessian differences are predominantly isotropic at 6–12 km support, separating processing effects from axis orientation. All six outer curvature roots lie within 0.702 km of the frozen 2011 front, the best placement among 65 parallel translations. Upward continuation preserves the central saddle in 100/100 realizations to 12 km, while the external root migrates and disappears near 4 km at standard support. A recovered scalar–triaxial file preserves the geographic contrast on reciprocal traverses. The surveys recover a structurally registered partial envelope and separate persistent geometry from processing-sensitive curvature. Historical line-offset sensitivity and external angular analogues delimit the result. Geographic vector closure and source mechanism remain unresolved.

1 Introduction

Three airborne magnetic surveys crossed the area around Uruana de Minas over four decades, but each preserved the field differently: sparse historical residual profiles in 1971–1972, regional grids and an original scalar–triaxial file in 2008, and raw flight-line observations in 2011. Such archives should not be expected to reproduce scalar amplitude. Survey altitude, line spacing, sampling, acquisition direction, levelling, gridding and filtering determine which wavelengths and derivatives remain visible [1, 2, 3]. Edge position and derivative amplitude also vary with observation height, source interference and processing [4, 5]. The scientific opportunity is therefore more demanding than map-to-map resemblance: which spatial relationships survive when epoch, instrument, support and representation change? Repeated UAV magnetic campaigns show why temporal comparison can separate stable structure from changing state [6, 7], while modern inversion work emphasizes explicit control of representation-specific effects such as terrain response [8].

Curvature methods provide a compact way to describe such geometry. For a scalar field F(E,N), a local quadratic approximation defines the horizontal Hessian H, whose eigenvectors are principal-curvature directions and whose eigenvalues carry curvature sign. Curvature and structure-tensor methods are established tools for interpreting potential-field geometry and edges [9, 10, 11, 12]. Here we use the Hessian for a different inferential question: does a local magnetic eigenframe remain recognizable when survey epoch, spatial support and data representation change, and does that eigenframe correspond to an independently mapped structural grain?

Uruana first appears in the 2011 archive through a simple observation: inside a narrow northern cap, the measured total field falls toward the north although the IGRF rises; farther north, the measured field rises again. That reversal is visible on every usable line before any Hessian or structural comparison is introduced. The older archives then ask whether the same location preserves a recognizable geometry. Project 1009 supplies 1971–1972 historical profiles, Project 0032 supplies a 2008 grid and recovered original file, and Project 3087 supplies the raw 2011 flight lines. We use them in sequence to test whether the sign change belongs to a coherent front, whether independently reconstructed walls occupy opposite sides of a fixed annulus centered near Uruana, whether the organizing frame follows mapped geology, and which three-dimensional source models remain admissible.

The practical question is which properties of a crustal magnetic boundary remain interpretable when historical and modern archives differ in amplitude, sampling and processing. We test geometric persistence against independently mapped structural grain, withheld flight lines, geographically wrong structural references and recovered sensor records. The resulting workflow separates reproducible spatial organization from representation-sensitive curvature and identifies where additional field measurements are needed. Transfer to other regions requires the same support and sensitivity checks; this case does not establish universal invariance.

The anomaly is a localized scalar-gradient departure from the main-field expectation and same-survey controls. Antipodal walls are dT/dN zero crossings in the fixed 7–9 km annulus at bearings 180° apart. Structural locking denotes alignment of the negative-curvature axis with mapped grain across epochs and supports. The partial envelope comprises observed opposed sectors and midpoint geometry; it does not imply azimuthal or vertical closure, shielding or magnetic-polarity reversal.

The present study and our related cross-survey manuscript [13] address distinct primary research questions. That manuscript tests whether a localized raw scalar-gradient reversal is directly observed and how a signed transition can be compared across heterogeneous survey supports and observation operators. Here the primary question is whether the spatial organization of the partial gradient envelope persists across decades and aligns with independently mapped geological structure. The corresponding tests concern opposed-wall midpoint geometry, signed curvature eigenframes, wrong-fabric and held-out-domain controls, and outer-root registration to the 2011 front. The shared survey observations provide the empirical anchor; the structural geometry, its controls and its interpretation constitute the contribution examined here.

Regional ranks are descriptive robustness screens and are not multiplied. The full scientific development is retained in Supplementary File S3, with its original section, table and figure numbering; Supplementary Files S1 and S2 provide complementary methods and reproducible outputs. The condensed main text retains the principal findings and inferential limits.

2 Geological, geographic and survey setting

Uruana lies in northwestern Minas Gerais within the western São Francisco craton/foreland context adjacent to the Brasília Belt [14, 15]. Structural constraints come from the 1:100,000 Buritis geological sheet [16], which spans a transition from stronger western deformation to less deformed central/eastern terrain. The 2015 Buritis report describes the east-verging São Domingos reverse-fault system placing Paranoá Group sandstone-bearing successions over Bambuí Group rocks. In the southwestern sheet, a separate NW-trending reverse fault places Lagoa do Jacaré Formation limestone over Serra da Saudade Formation siltstone and sandstone. These mapped units and structures provide the geological setting; the length-weighted structural grain used below summarizes multiple traces rather than identifying a single fault or lithological contact. Municipal population and administrative history [17, 18] are contextual only.

The magnetic datasets are kept separate. Project 1009 (1971-72; [19]) supplies historical PGW residual profiles that are predominantly east-west near Uruana. Project 0032 São Francisco (2008; [20]) supplies 1.5-km regular grids of raw magnetic field (Mag) and a diurnal-corrected representation (mag_var). Project 3087 (2011; [21]) supplies raw scalar total-field flight-line measurements from which target slopes, same-line northern controls and free breakpoints are recovered. Table 1 summarizes the role of each dataset.

Table 1
Datasets and inferential roles

Dataset	Representation	Primary role
1971-72 Project 1009	Historical PGW residual profiles, mainly E-W locally	Historical antipodal-wall holdout; line-gradient ladder; Hessian
2008 Project 0032	1.5-km Mag and mag_var grids	Antipodal-wall replication; +/−/+ topology; Hessian; scale ladder
2011 Project 3087	Raw scalar total-field N-S flight lines + IGRF	Direct gradient reversal; free turnover front; regional strict gate
Buritis 1:100,000 GIS	Mapped S-surface traces + contractional/reverse faults	Independent structural grain and scale tests
SRTM / gravity / gamma products	Independent cross-domain fields	Negative controls and inference boundary
WorldCover / ANM / ANEEL / OSM	10 m land cover and mapped infrastructure	Independent 8/16 km anthropogenic-confounder screen

3 Data and methods

3.1 Raw field anchor and independent survey topology

Project 3087 observations were aggregated into 250 m northing bins. A line was eligible with at least five bins and 1 km support in the fixed + 6 to + 8 km northern target cap; fourteen north–south lines qualify. Raw field was regressed against northing, and IGRF-14 [22] was evaluated at the survey epoch and

matching support. The same lines were tested in the 16–20 km northern control. A strict signature requires negative target slope, positive control slope, positive IGRF gradients in both zones and a freely optimized negative-to-positive two-segment breakpoint. The fourteen breakpoint coordinates remain frozen. These same-line contrasts avoid between-line zero-level differences. IGRF represents the broad core field; its degree-13 bandwidth cannot supply the local 8–20 km structure.

For Project 0032, four successive northward intervals are fixed relative to each candidate center: 0–8, 8–16, 16–24 and 24–32 km. Uruana exhibits the sign sequence + - + + in both Mag and mag_var. The regional robustness gate applies five longitude-corridor half-widths (0.75, 1.5, 3, 6 and 9 km) to both channels. A 2008 pass requires the + - + + sequence in all ten realizations. Candidate centers lacking complete 0–32 km 2008 support are not adjudicated by this gate. The strict 2011 and robust 2008 gates are defined separately before intersection.

The regional baseline uses a non-overlapping 16 km lattice, with 97 eligible 2011 centers and 82 having complete 2008 support. A reduced implementation has 96 centers but recovers the same strict passes and cross-survey intersection (S3 Sections 3.1–3.2). A smooth line changing gradient sign must cross dT/dN = 0; the fitted breakpoint estimates the front organization rather than a pointwise zero coordinate.

3.2 Opposed walls and historical prediction

The municipal-seat coordinates of Uruana and the 7–9 km annulus were fixed before the antipodal test. The 7–9 km band was defined as a ± 1 km tolerance around the pre-existing 8 km target radius used in the independent 2011 analysis; it was fixed before wall counting and was not selected from the antipodal result. For each 2008 grid representation, dT/dN was sampled on 360 one-degree radial spokes after Gaussian smoothing at 1.5, 3.0 and 4.5 km. A wall was recorded where dT/dN crossed zero within the annulus. Bearings separated by exactly 180 degrees were paired, and we recorded pair count, longest consecutive axial run, opposed-radius mismatch and the midpoint of representative walls. The full horizontal-gradient winding number—the signed net number of complete rotations made by the horizontal-gradient vector along a closed circuit—was measured on concentric circles to distinguish opposed derivative walls from a centered static scalar-field extremum.

Historical Project 1009 PGW is an IGRF-reduced residual product. For each historical realization, an approximate total field was reconstructed by adding the independently evaluated historical IGRF scalar field at the archived survey epoch and altitude before applying the same radial dT/dN = 0 wall operator.

Identical annulus operators were applied to 533 modern and 704 historical eligible centers. Eighteen historical realizations cross interpolation, grid spacing and smoothing; six modern realizations cross two channels and three smoothing scales. Their 108 matched pairs use 407 complete-support controls. A control survives when it equals or exceeds both corresponding Uruana wall counts. Uruana self-comparison supplies no evidence. Treatment-wise factorization and sector concentration were examined after the sweep; spatial dependence prevents treating their counts as calibrated probabilities (S3 Section 3.2.4).

Within an 8-km circle, historical east–west lines require five points, 4 km east–west span and greater east–west than north–south extent. PGW slopes against easting are ordered by mean northing; regional controls on the same 16-km lattice require eight lines. Ordering and within-line correlation are tested without amplitude rescaling (S3 Section 3.3).

Using the same 73 points on eight historical lines, we compare a plane, a bilinear model (1, E, N, EN), two five-parameter models and the full quadratic. Each complete line is withheld in turn; the primary score pools squared errors over all withheld points, with other line-error summaries retained in S2. OLS, Theil–Sen, endpoint estimates and omissions test the northward trend of east–west slopes. Constant line offsets preserve those slopes, whereas line tilts do not. A separate optimization finds the minimum equal-line RMS of zero-sum offsets needed to reach det(H) = 0. This is a retrospective sensitivity boundary, not measured levelling error.

3.3 Hessians and boundary registration

Centered local coordinates E and N in kilometres are fit with $F(E,N) = a + bE + cN+dE^2+eEN + fN^2$. The horizontal Hessian is H=[[2d,e],[e,2f]]. The off-diagonal element e is the mixed partial HEN; eigenvectors provide axial principal-curvature directions and eigenvalues provide curvature sign. Because axes are axial, all orientation differences are reduced modulo 180 deg. For the standard linearized total-field anomaly above its sources, the harmonic potential-field relation gives TEE + TNN+Tzz = 0. We therefore recover the scalar vertical second derivative without using any fluxgate axis as Tzz=-tr(H). This derived quantity is vertical curvature of the scalar anomaly, not the geographic magnetic-vector component Bz.

Quadratic fits use 2008 radii 6, 8, 10, 12, 16 and 20 km in both channels. Sliding Hessians along the fixed + 2 km east track identify HEN = 0 and det(H) = 0 roots at 6, 8 and 10 km support. Six outer roots are compared with the frozen 2011 PCA line in common UTM coordinates. Maximum absolute perpendicular separation is the primary placement score; mean separation is secondary. Keeping orientation fixed, the line is translated from − 8 to + 8 km in 0.25 km increments, giving 65 positions. This deterministic comparison tests placement conditional on orientation, not a p-value, rotational specificity or source depth (S3 Section 3.4).

3.4 Geological frame and orientation controls

The local structural grain is estimated from the Buritis GIS using mapped S-surface traces and contractional/reverse faults, without lithologic contacts. Line segments are weighted by length and summarized by an axial circular mean. The principal analysis uses a 20-km radius; the axial mean-resultant-length statistic R_ax measures directional organization. Two scale stresses are then run mechanically: (i) geology fixed at 20 km while the magnetic Hessian radius varies 6–20 km; and (ii) the 8-km magnetic Hessian fixed while structural buffers vary 10, 15, 20, 25 and 30 km. The angular mismatches are point estimates. R_ax describes directional concentration, not uncertainty in the mean axis; the support ladders quantify scale sensitivity rather than confidence intervals.

To test whether the structural grain acts as a natural coordinate frame for magnetic curvature, H is rotated from geographic E,N coordinates into U,V coordinates with U parallel to the mapped structural axis and V perpendicular. We quantify the off-diagonal fraction q=|HUV|/||H||F and the collapse C = 1-qUV/qEN. A value C near one indicates that most apparent mixed curvature in E,N disappears after rotation into the structural frame. The test is applied to both 2008 channels, the 2008 scale ladder and the 1971 historical Hessian. Because the structural frame comes from an independent mapping product, this is not an algebraic eigenvector rotation chosen to diagonalize H.

At 28 geology-overlap centers, the fixed 8-km raw and corrected magnetic axes are compared with all 28 mapped structural axes. Without optimizing a continuous rotation, this empirical wrong-fabric substitution asks whether the geographically correct structure matches its Hessian better than plausible regional alternatives.

Second, three independent orientation domains are placed on the same axial 0-180 deg space: the 1971 negative-curvature Hessian axis, the mean 2008 negative-curvature axis from raw and corrected grids, and the mapped geological structural axis. In leave-one-domain-out reconstruction, two domains reconstruct the third by their axial circular mean; the endpoint is the largest of the three held-out errors. This uses 28 common-support centers and fits no free consensus angle to all three simultaneously.

A four-domain extension adds the 2011 front normal, obtained by adding 90° modulo 180° to the endpoint or PCA front axis. Each domain is reconstructed from the other three; the conservative endpoint is the worse result across the two front definitions. Nine centers have complete four-domain support (S3 Section 3.8).

Signed-frame checks require the structural direction to follow the negative-curvature branch and det(H) < 0 in the historical fit and all twelve modern channel-by-radius fits. Two historical Hessian implementations serve separate bridge and structural-frame analyses; their axes differ by 0.2574°, and their values are kept distinct (S3 Sections 3.5–3.9). Cross-domain holdouts are retrospective internal consistency tests, rather than prospective prediction of an unseen dataset.

3.5 Processing and vertical scale space

To audit processing effects, each 2008 Hessian is decomposed as H = S+[tr(H)/2]I, where S is traceless and contains the axis orientation and eigenvalue gap. The squared Frobenius norm of a raw-to-corrected difference separates into $||\Delta S||^2+[\Delta tr(H)]^2/2$. Where compact source tables retain only trace magnitude, both trace signs are evaluated and the isotropic energy fraction is reported as a bound. Bearings are measured clockwise from north, with eigenvectors represented in (E,N) coordinates as (sin θ, cos θ). This diagnostic describes differences between two products of one survey; it is not an independent temporal or source-mechanism test.

Upward continuation follows the central Hessian over two channels, two detrending choices and 25 levels from 0 to 12 km. The external determinant-root family is tracked separately on its fixed east-offset

trajectory, with boundary treatments and Hessian supports varied. Continuation is a spatial filtering operator; its levels are not measured flight heights or estimates of source depth (S3 Section 3.9).

3.6 Original sensor records and geological context

The original 0032_SAO-FRANCISCO_MED_PROC_00237.ASC file was recovered from ANP IBM 3592 media and verified against archive metadata (filename, byte size, MD5 and record count in S2). It contains simultaneous scalar mag1 and triaxial fluxgate fX, fY and fZ observations. The norm Fflux= $(fX^2+fY^2+fZ^2)^{1/2}$ is invariant to rigid sensor-axis rotation. Consecutive lines 10 and 20 cross the pre-existing São Domingos structural trace in opposite flight directions. Crossings and side windows were fixed before inspecting Fflux (S3 Section 3.2.1).

East-minus-west mean steps were calculated in 0.5–3.0 km windows separated by a 1 km exclusion. Robustness crossed nine fixed window pairs (inner 0.5, 1.0, 1.5 or 2.0 km as applicable; outer 2, 3 or 4 km) with two coordinate treatments: records carrying explicit GPS positions (~ 1 Hz) and sensor-rate records (~ 10 Hz) whose positions were linearly interpolated only between bracketing GPS epochs. Spatial selectivity used the identical operator at 1 km-spaced centers along line 10 and within ± 100 km. Stored fX/fY/fZ remain sensor axes and are never individually renamed as geographic components.

Reciprocal lines separated by 5.989 km supply matched-meridian scalar and fluxgate-norm finite differences, with their midpoint 7.110 km north of Uruana inside the 2011 cap. Regional calibration excludes the target. Directional decomposition and geographic cross-derivative closure are diagnostic tests only: absent true roll, pitch and mounting calibration, stored axes cannot establish definitive geographic vector components (S3 Section 3.2.1).

An orthogonal tie-line supplies an additional 2008 intercept acquired 63 days earlier. Three-flight gradient reconstruction keeps intercepts acquired on different dates separate, solves horizontal components using observed side-window centroid displacements and compares nine fixed-window axes against four frozen 2011 front definitions (S3 Sections 3.2.2–3.2.3). Along-fault tests use identical windows at successive São Domingos crossings. A retrospective mineral-occurrence score with commodity labels withheld supplies spatial context, not a mineral-discovery or source-causation test (S3 Section 3.6.1).

We screened mapped human infrastructure around the frozen center (16.0593° S, 46.2585° W) without changing the pre-existing spatial design. The 8 km target disk remained primary; a 16 km disk was used only as a sensitivity envelope. Built-up and rural land-cover fractions were calculated from the 10 m ESA WorldCover 2021 v200 product [27]. Major energy infrastructure was queried from ANEEL transmission-line and substation services and the SIGA generation register [28, 29]. Active mineral-process polygons were intersected from ANM SIGMINE with legal phase retained, because a process polygon does not establish an operating mine [30]. OpenStreetMap/Overpass supplied a supplementary inventory of settlements, major roads, towers, aerodromes and tagged industrial, quarry and power features [31].

Infrastructure tests ask whether mapped installations have the scale, geometry and chronology needed to explain a response across survey generations. Present-day layers do not reconstruct 1971; absence

from volunteered maps is corroborative only. Official ANEEL and ANM records provide the principal tests, without excluding small objects, distribution wiring or unmapped features.

3.7 Controls reproducibility and literature screen

An external operator control uses a metadata-ranked Alaska survey pair selected before confirmatory values were inspected: South National Petroleum Reserve 1977 and Howard Pass 2008 [23–26]. The unsigned eigenframe hypothesis, 20 km support, selection rule, 899-rotation reference and pass thresholds were frozen prospectively. It tests recoverability of geographic correspondence across heterogeneous surveys, not transfer of the Uruana anomaly (protocol and genealogy in S1/S2).

After that outcome, an exploratory search applied Uruana-derived axis-mismatch and normalized-spectrum thresholds to Alaska double-saddle centers, then refitted selected cases at multiple supports. Separately, epoch-factorized and spatially shifted antipodal controls diagnosed dependence among the Uruana screens. Thresholds, support failures and outputs are retained in the exploratory S2 addendum; these follow-up checks are retrospective.

The literature screen completed on 10 September 2026 used Crossref, OpenAlex and publicly indexed literature, combining airborne scalar-gradient reversal, main-field opposition, repeated surveys, reciprocal lines and scalar–vector corroboration. Titles, abstracts and accessible full texts were screened. Coverage excludes a systematic census of non-English, proprietary, unindexed or unpublished archives; documentary novelty is restricted to the searched corpus (S3 Section 3.12).

All primary measurements are public third-party data. Supplementary File S2 contains the frozen 2011 breakpoints, complete regional-control tables, structural-frame and leave-one-domain-out tables, the new vector-file audit and deterministic verification scripts. The newly recovered upstream file is identified by filename, byte size and MD5 but is not redistributed.

OpenAI ChatGPT (accessed August–October 2026) was used only as an assistive tool for language editing, code drafting and debugging, and audit organization. The authors conceived the study, defined the methods and inferential rules, selected and verified the data, reviewed all code and outputs, independently confirmed the reported values, interpreted the results and approved the final manuscript. The authors retain full responsibility for the work. No generative-AI images were used.

4 Results

Three findings support the geological interpretation: opposed-wall geometry recovered from the historical and modern grids (Section 4.2), reconstruction between magnetic and independently mapped geological orientations (Section 4.4), and the geographic contrast retained in recovered scalar and fluxgate records (Section 4.6). The 2011 reversal fixes the geographic anchor (Section 4.1). Boundary placement and processing tests assess how these relationships survive different representations (Sections 4.3 and 4.5), while Section 4.7 bounds documentary novelty.

4.1 Raw reversal and bounded survey topology

The geographic anchor requires no derived geometry. All 14 usable 2011 lines have negative raw northward slopes in the target (median − 1.555 nT km − 1) despite positive IGRF gradients (+ 0.993 nT km − 1). The same lines recover positive raw slopes farther north (+ 0.963 nT km − 1), with positive IGRF gradients there too. Every paired raw change is positive. Figure 1 shows the line-level contrast.

Free two-segment fitting recovers a negative-to-positive breakpoint on all 14 lines. The frozen breakpoint chain has an exact endpoint axis of 61.776 deg and PCA axis of 63.688 deg. These coordinates are the site-level geometric anchor for later comparisons; they are not moved after geological inspection. Figure 1 shows the paired raw slopes and the frozen front geometry.

After IGRF subtraction, median residual slopes are − 2.607 nT km − 1 at the target and + 0.267 nT km − 1 in the northern control. Every within-line control-minus-target residual contrast is positive. Six of 97 regional centers meet the strict signature. Complete contrasts are retained in S3 Section 4.1.

The broader 2008 intervals supply a separate bounded topology. Raw and corrected grids both recover + − + + northward slopes across four successive 8-km intervals and all five fixed corridor widths. Their positive 0–8 km slope does not contradict the narrower negative 2011 + 6 to + 8 km target slope: the supports and estimators differ (S3 Section 4.2).

Among 82 centers with complete support, four meet the robust 2008 gate; intersecting it with the strict 2011 gate leaves Uruana alone. The reduced 96-center implementation recovers the same intersection. This intersection identifies the regional site for subsequent geometry tests.

4.2 Persistent opposed walls and historical sensitivity

The annulus test asks whether older archives recover a coherent spatial form at that site. Both 2008 channels preserve north–northeast and south–southwest dT/dN = 0 walls in the fixed 7–9 km annulus at all three smoothing scales. Representative opposite-wall segments have midpoints 0.300–1.207 km from Uruana. The canonical corrected field gives 18 consecutive antipodal axes at 13–30°, and raw Mag gives nine axes (Fig. 2; full radii, mismatch values and regional distributions in S3 Section 4.3).

Restoring the independently audited main-field gradient to the historical PGW residual recovers opposed walls in all 18 historical realizations; PGW alone has no annular pair. The canonical reconstruction gives 12 consecutive axes at 21–32°, a 0.647 km radius mismatch and a midpoint 0.162 km from Uruana. Ten consecutive axes overlap canonical 2008.

No control among 407 complete-support centers equals or exceeds both canonical epoch counts. Across all 108 specification pairs, only eight controls ever exceed both thresholds, and none survives more than 36 pairs. All 36 pairings using corrected 2008 fields at 3.0 or 4.5 km smoothing have no exceeding control. Figure 2 and S3 Section 4.3 retain the complete regional robustness sweep.

All canonical wall pairs cross in the same radial direction: 12/12 historical, 9/9 raw-2008 and 18/18 corrected-2008 axes. At 3–4.5 km smoothing, inner samples belong to the connected positive-dT/dN component containing Uruana; outer samples generally occupy separate negative components. Horizontal-gradient winding is zero at every tested radius, scale and channel, rejecting the simplest centered static scalar extremum. The eight occasional translated survivors occupy one 23.199° sector (Fig. 2; full post-discovery footprint analysis in S3 Section 4.3).

Eight historical east–west lines show strictly increasing slopes from south to north, with median within-line $|r|=0.9964$. The ordering is uncommon in the regional controls and survives 22/25 center shifts within ± 2 km. Full historical ordering and modern affine-row endpoints are retained in S3 Section 4.4.

Historical reconstruction does not reproduce the 2011 window-averaged total-field inversion: restoring either retrospective or acquisition-era IGRF leaves the historical mean total gradients positive. Conversely, degrading 2011 to historical-scale resolution retains inversion on all 14 lines. IGRF generation and coarse resolution alone therefore do not explain the different gradient states. Residual-product provenance and unmatched support remain limitations (S3 Section 4.4; exploratory S2 addendum).

Withholding complete historical lines reduces pooled RMSE from 5.00 nT for a plane to 3.34 nT for the bilinear model, a 33.2% improvement. Additional quadratic terms improve training fit but not this pooled prediction score; a five-parameter model wins on mean and median line error, so bilinear superiority is score-dependent. The northward trend of east–west slopes remains positive under all point and whole-line omissions. Full quadratic saddle classification is less robust: constructed zero-sum line offsets of equal-line RMS 4.543 nT reach $\det(H) = 0$. These offsets are sensitivity limits, not measured errors. The slope trend therefore survives nuisances that can remove the historical saddle (complete model and omission tests in S2 and S3 Section 4.4).

4.3 Outer curvature boundary and the later front

Across 6, 8 and 10 km Hessian radii and both 2008 channels, the first $\mathrm{HEN} = 0$ family occurs at 5.84–6.54 km north, the first $\det(H) = 0$ family at 12.30–13.49 km and the second $\det(H) = 0$ family at 18.74–20.22 km. In common UTM geometry, all six outer roots fall within 0.702 km of the frozen 2011 PCA front; their mean absolute perpendicular separation is 0.358 km, and their ensemble-mean signed position is − 0.032 km from the line.

Among 65 parallel translations at frozen orientation, the real 2011 front has the smallest maximum and mean absolute separation from the six outer 2008 roots. The nearest competitor increases maximum separation from 0.702 to 0.873 km. The result establishes geometric registration across both 2008 channels and all three supports at the frozen front orientation.

The ordered $\mathrm{HEN} \rightarrow \det \rightarrow \det$ root sequence is common regionally and does not carry the inference alone. Combining it with positive historical mixed shear and robust 2008 turnover leaves Uruana alone

among 39 ordered centers. Figure 3 shows the architecture; its strongest boundary evidence is registration to the later front. Exact spacings and phase-balance controls are retained in S3 Section 4.5.

4.4 Independent geological alignment and reconstruction

The independently mapped structural grain is 146.255° within 20 km (R_ax = 0.740). The 8-km 2008 negative-curvature axes are 145.571° and 147.415°, a maximum mismatch of 1.160°. Among 28 common-support centers, Uruana has the closest alignment. Greater structural concentration does not itself explain the match: the most concentrated nearby center is almost orthogonal to its magnetic eigenframe (S3 Section 4.7).

The independent direct 2011 front is transverse to this fabric. The structural axis differs from the exact endpoint front by 84.48 deg axially, only 5.52 deg from a perfect perpendicular; the exact PCA front is 82.57 deg from the fabric, 7.43 deg from perpendicular. Thus one 2008 Hessian eigenaxis follows the crustal grain and the orthogonal curvature family points toward the later turnover-front orientation.

The high-resolution front-on-structure holdout does not pass every pre-frozen localization criterion and is not used to claim that the 2011 front sits on one mapped fault. The promoted result is different: a post-discovery but quantitatively regionalized alignment between the local magnetic eigenframe and the independently mapped structural grain. This distinction is retained in the claims matrix. The cross-domain structural locking and scale sensitivity are shown in Fig. 4.

The alignment survives changes in magnetic support. With geology fixed at 20 km, all twelve 2008 channel-by-radius fits remain saddles; their worst mismatch across 6–20 km is 7.553°, the smallest regional worst mismatch. Removing the smallest support preserves this position.

It also survives changes in geological support. With the magnetic Hessian fixed at 8 km, structural buffers of 10–30 km give axes of 144.83–147.68° and a worst mismatch of 2.586°. Thus neither scale ladder depends on one selected radius (full ranks in S3 Section 4.8).

Rotating the magnetic Hessian into the independently mapped structural frame reduces the 8-km off-diagonal term by 97.44% in raw Mag and 95.54% in mag_var. The collapse remains at least 73.72% across 6–20 km. Because geology supplies the rotation, this is an external-frame test rather than an eigenvector rotation that diagonalizes by definition (Fig. 5; S3 Section 4.9).

The same frame reduces historical off-diagonal curvature by 92.04%, with the historical negative axis 2.168° from the mapped fabric. Only Uruana jointly meets its historical and modern multiscale diagonalization thresholds among the 28 centers. This links the older and modern fields to a common geological reference (Fig. 5).

Geographically wrong fabrics test whether a broadly regional strike could produce the match. Of 28 mapped alternatives applied to the fixed Uruana Hessian, the local fabric is closest: 1.160° mismatch

versus 3.370° for the best wrong fabric. Uruana also has the strongest own-fabric specificity across the regional centers (S3 Section 4.10 and S3 Fig. 8).

Holding out an entire orientation domain tests reconstruction rather than simultaneous alignment. Any two of geology, the historical magnetic axis and the modern magnetic frame reconstruct the third with a worst error of 2.287°. Uruana ranks first among 28 supported centers; the next center has 24.263° error. Figure 6 shows the three holdouts. The holdouts recover a common reference frame without fitting a consensus angle to all three domains.

Adding the 2011 front normal raises the conservative worst held-out error to 9.899°, with the largest error when that normal is withheld. The older magnetic and geological domains reconstruct one another more closely. The front is therefore related to the persistent frame without being forced to share its exact orientation (S3 Section 4.11 and S3 Fig. 10).

The full wrong-fabric, signed-frame and four-domain control tables are retained in S3 Sections 4.10–4.13 and Tables 2–3. Partial regional competitors reproduce individual angular descriptors but fail the robust 2008 topology or local geological alignment; such partial matches limit interpretation of any one regional rank.

4.5 Persistent frame and variable curvature state

Frame persistence is meaningful only if it can be separated from curvature state. The historical fit and all twelve modern channel-by-radius fits are saddle-like, with the structural direction following the negative branch. The historical alignment is 2.168° and the worst modern alignment is 7.553°; the signed-frame control tables are retained in S3 Section 4.12.

The balance between the two curvature branches nevertheless changes. Historical negative curvature dominates (|lambda−|/lambda + = 3.01), whereas positive curvature dominates both 8-km modern products (ratios 0.36 and 0.53). The Hessian trace changes sign, so Tzz = − tr(H) changes from positive to negative. The negative eigenaxis stays near 144–147°. The persistent observable is the organizing frame and saddle topology, not a stationary curvature spectrum.

The historical-to-corrected-2008 frame rotates by 3.328° while normalized spectrum-shape distance is 0.744. Among 28 common-support centers, only Uruana combines an equal-or-smaller rotation with an equal-or-larger spectrum change while retaining both saddles. The regional frame-spectrum comparison is retained in S3 Section 4.12.

Processing helps explain why state and frame must be distinguished. Isotropic curvature accounts for at least 86.26% of raw-to-corrected squared Hessian-difference energy at 6–12 km support, but not at 16–20 km. Across all six radii, eigenvalue-gap change remains below 2.00% and axis rotation at most 2.501°. Isotropic shifts preserve axes and gaps while permitting eigenvalue-sign and topology changes. Such classification changes occur regionally, whereas all twelve Uruana fits retain saddle topology (complete bounds in S3 Section 4.12 and S2).

Upward continuation separates the central saddle from the outer boundary. All 100 central realizations remain saddles through 12 km of continuation, but the outer determinant root migrates and disappears near 4 km at standard 8-km support. Its disappearance level varies from 1.625 to 6.125 km with Hessian support and cannot be interpreted as source depth. Trajectory interception is common regionally, so native-scale placement remains the stronger boundary result (S3 Section 4.12).

External controls limit the interpretation of this persistence. The prospectively frozen Alaska operator test passes its declared criteria for recoverable geographic registration. The subsequent exploratory search finds angular analogues under substantial spectrum change, including one stable double-saddle case at 16 and 20 km. Inadequate smaller-support coverage prevents full architectural matching, but axis stability alone is not unique to Uruana. Protocols, coverage checks and external-control outcomes are retained in S3 Section 4.13 and the exploratory S2 addendum.

Negative tests define the surviving interpretation. A centered stationary scalar extremum and simple closed contours are not supported; topography, gravity and radiometrics do not reproduce the localized magnetic architecture. Historical mean total-field inversion is absent, and the outer root is not vertically stationary. The evidence supports a persistent native-scale boundary and geological frame, with azimuthal and vertical closure unresolved (S3 Section 4.13).

4.6 Sensor agreement and spatial localization

Recovered instrument records test whether gridding or flight direction could produce the apparent boundary. At fixed São Domingos crossings, scalar and fluxgate-norm east-minus-west steps retain the same positive sign on consecutive production lines flown in opposite directions. Their four standard-window estimates span 13.474–14.482 nT; within-line scalar–norm mismatches are 2.32% and 0.49%. A monotonic drift explanation would require opposite drift signs on the reciprocal lines. Full window, positioning and drift audits remain in S3 Section 4.14.

An orthogonal tie-line acquired 63 days earlier adds a different-date directional check. It crosses the same concealed São Domingos segment and gives a + 7.110 nT raw scalar increase toward the same northeastern side. It independently reproduces the side-of-boundary direction (Fig. 7).

The reciprocal pair also preserves the northward deficit at matched meridians. Target-minus-regional meridional-gradient residuals are − 2.109 nT km − 1 for scalar mag1 and − 2.094 nT km − 1 for the fluxgate norm, differing by 0.730% relative to the scalar residual. Both occupy the negative tail of identical translated controls. Their invariance to rigid sensor-axis rotation makes this the strongest corroboration from the recovered file. Housekeeping steps do not reproduce it (S3 Section 4.14).

A deliberately stronger waveform test fails. With no reflection, stretching, sign flip or target-dependent translation, constant-only detrending gives high correlations because the lines share a broad regional trend. After linear detrending, the local waveforms anticorrelate; at 8 km support, r is − 0.887 for mag1 and − 0.503 for Fflux. The repeated result is therefore the boundary location and east-minus-west contrast, not the detailed waveform of a single compact body. Figure 7 summarizes the reciprocal-flight,

dual-sensor boundary audit. The principal acquisition and sensor checks are summarized in Supplementary File S3, Table 4.

Directional decomposition is diagnostic only. Approximate calibrations retain a predominantly tangential response, but no tested reconstruction passes the illustrative geographic Maxwell-closure tolerance. Missing attitude and mounting calibration preclude a physical vector-field interpretation. Full rates, components and all 36 failed closure reconstructions are retained in S3 Section 4.15 and S2.

Boundary response is also localized along the mapped fault. Historical residual, gridded 2008 and recovered scalar/norm steps are close at the fixed crossing, but unmatched support prevents interpreting this as calibrated temporal amplitude invariance. Modern steps weaken along strike, and a nearby hematite occurrence provides a sampling target without establishing source causation (S3 Section 4.16).

The infrastructure screen finds a predominantly rural target and no registered major energy installation within 16 km. The sole active mineral-process polygon inside 8 km is a small clay licensing request, which does not establish extraction or magnetic source mass. These screens disfavor a major mapped installation as the common cause across survey generations, while leaving small local or unmapped objects unexcluded (S3 Section 4.17).

Finally, an independent scalar-gradient reconstruction from the three 2008 flights agrees with the 2011 front across the full window-by-front comparison envelope, with maximum angular mismatch 2.193°. A nominal 0.015° pairing is not an accuracy claim. Together with the fourteen line-level sign changes, this supports a coherent directional-derivative front (S3 Sections 4.18–4.19).

S3 Sections 4.14–4.19, Tables 4–5 and Figs. 13–17 retain the full sensor, vector, along-fault and environmental audits. The recovered original sensor records corroborate the geographic contrast and distinguish boundary persistence from waveform similarity.

4.7 Scope of documentary rarity

The literature screen found relevant comparators but no full documentary analogue in the searched corpus. These include Bangui's long-wavelength multichannel anomaly [32], Kursk's large-area magnetic-gradient mapping [33], Jõhvi's remanently magnetized iron ore [34], German regional vector-anomaly mapping [35], scalar–vector survey equivalence [2] and orientation-sensitive towed vector measurements [36]. The documentary result concerns the full conjunction of raw-gradient opposition, same-line recovery, cross-epoch wall geometry and reciprocal scalar–triaxial agreement.

5 Discussion

5.1 Interpreting heterogeneous magnetic archives

The geological value of this case is that spatial organization can remain recoverable when the archives do not reproduce amplitude or curvature state. The independently mapped structural frame nearly diagonalizes both historical and modern Hessians, and two orientation domains reconstruct the third within 2.287°. Withholding complete historical flight lines also favors a mixed spatial term over a plane on the pooled error criterion. These checks make the geological association testable without requiring identical field levels or treating every fitted descriptor as a physical source parameter.

This distinction matters when legacy surveys are reused for structural interpretation. A mismatch in amplitude does not automatically invalidate a shared boundary, while agreement in one angle does not establish that the same physical source has been uniquely recovered. Here, raw-to-corrected differences predominantly alter isotropic curvature at local support, whereas principal axes and eigenvalue gaps remain comparatively stable. The processing audit therefore identifies which properties can support a geometric comparison and which require representation-specific qualification. Larger supports do not share the same isotropic dominance.

The result supplies a reproducible workflow for comparing magnetic archives against independent geological structure. Other regions require independent geological constraints, adequate common support, treatment-specific processing audits and controls for plausible alternative structural axes. The Alaska analogues show that stable axes with substantial spectrum change also occur elsewhere. Uruana's specificity lies in the conjunction of geological registration, opposed walls, the later reversal front and recovered sensor records, rather than axis stability alone.

5.2 Geological interpretation and follow up measurements

The data favor a spatially fixed crustal magnetic-property boundary associated with the mapped structural grain. Adjacent reciprocal lines preserve geographic step and location while their detrended local waveforms anticorrelate. This is compatible with varying magnetization along strike and explains why a repeated boundary need not have a repeated compact-body waveform. Susceptibility contrasts, remanence, fault-related alteration and interacting boundaries at depth remain viable. The nearby hematite occurrence gives a concrete sampling context, but its presence does not demonstrate a mineralogical cause.

The persistent bilateral midpoint and native-scale registration of outer roots to the later front constrain where new measurements should be made. Ground magnetic vectors and susceptibility/remanence sampling should cross the mapped São Domingos sector and its weaker along-strike continuation. Orthogonal and oblique profiles should cover the unsampled azimuths of the 7–9 km walls and the outer 12–20 km transitions. Multiple measured heights, simultaneous inside/outside stations and attitude-calibrated geographic vectors would distinguish spatial closure, depth-dependent response and temporal coherence. S3 Section 5.13 and Supplementary File S3, Fig. 18 retain the complete campaign and competing-source predictions.

A partial gradient envelope is supported, but the centered static scalar-extremum model fails the winding and contour tests. A closed shell, non-axisymmetric dome or dynamic vector envelope remains a hypothesis alongside dipping or juxtaposed magnetic domains. Geographic Maxwell closure fails under available approximate calibrations. Directional deflection therefore does not establish circulation, shielding, field-line rotation or protective, biological or atmospheric effects.

5.3 Dependence rarity and limitations

Regional screens share data and their ranks cannot be multiplied. Nested phases, signed frames, structural alignment and domain holdouts probe different failure modes of overlapping archives. Their evidential weight lies in stability under specified transformations and controls, rather than accumulated probabilities. Epoch factorization makes this dependence explicit: historical survival is more frequent among modern-surviving controls, but no control survives every modern specification. Consequently, zero survivors across all 108 pairs are constrained by the modern endpoint and are not a further independent confirmation. Uruana self-comparison passes by construction and supplies no evidence. Complete conditional frequencies and spatial-shift diagnostics are retained in S2.

The literature search found no full documentary analogue within its accessible corpus, but that cannot establish worldwide physical uniqueness. Historical and modern magnetic products have different observation supports and provenance. Most geometry tests were developed after discovery; the historical line and orientation holdouts are internal retrospective checks. Shared aircraft and acquisition geometry limit the independence of scalar–fluxgate corroboration, and flight heading remains confounded with line identity. Spatially correlated map segments and magnetic grid cells have not been jointly resampled to obtain angular confidence intervals. The numerical ordering of nearby angular mismatches therefore does not establish statistically resolved differences between fabrics. The geological map was compiled before this analysis and independently of our magnetic target and eigenframe fits, but its compilation included regional geophysical products; independence here does not imply statistically independent source information.

Historical constant line offsets leave the within-line slope trend intact, but coordinated synthetic offsets can remove quadratic saddle classification. The full quadratic stationary point is 14.143 km from Uruana, outside the sampled 8 km convex hull; whole-line omissions retain distances of 11.409–18.519 km outside their respective hulls. Hessian orientation does not locate a physical source center. Nearby-center tests also retain the fixed Uruana geological axis rather than remapping geology at every position. External analogues lack the smaller-support coverage needed for full architectural matching; failed spatial-shift support and the unexecuted next survey pair supply no inference. S3 preserves every secondary endpoint, negative result and its dependency boundary.

6 Conclusions

The Uruana archives recover a persistent geological reference frame across four decades despite differences in magnetic amplitude and curvature state. Opposed directional-derivative walls retain near-

Uruana midpoint geometry, historical line prediction improves over a plane, and magnetic and independently mapped geological domains reconstruct one another within 2.287°. The outer 2008 curvature boundary registers to the independently frozen 2011 front, while recovered scalar and fluxgate-norm records retain the geographic contrast on reciprocal traverses.

The practical contribution is a tested separation of reproducible structural geometry from processing-sensitive scalar curvature in heterogeneous magnetic archives. That separation supports geological interpretation and directs follow-up measurements. External angular analogues, historical offset sensitivity and failed geographic closure limit claims of uniqueness and three-dimensional structure. The evidence characterizes a structurally registered partial envelope and supplies specific observations that future source models must reproduce.

Declarations

Related manuscripts and preprint disclosure

This manuscript and our related submission to Acta Geophysica (AGPH-D-26-00880) are distinct studies with different primary research questions, analytical endpoints and principal conclusions. The Acta study concerns direct detection of the raw scalar-gradient reversal and operator-aware comparison of signed transitions across heterogeneous surveys. The present study concerns the persistent geometry and geological alignment of the partial gradient envelope. Its principal endpoints are opposed-wall midpoint geometry, cross-epoch curvature-frame alignment with 1:100,000 geological mapping, empirical wrong-fabric and held-out-domain tests, and outer-curvature-root registration to the frozen 2011 front.

Both studies use the same public survey archives and share baseline observations of the 2011 reversal and northern recovery, the 2008 turnover, historical derivative corroboration and scalar observations near the São Domingos structure. These shared observations establish the geographic and empirical anchor; they are not presented here as a second independent discovery of the reversal. The present manuscript develops the distinct structural-geometry question and adds reciprocal two-sensor and rotation-invariant analyses. The material identified in this disclosure comes from our own related research and preprints, not from an article of ours previously published in a peer-reviewed journal.

The related work is publicly available as Ribeiro LG and Simonssini MA (2026), “Cross-Survey Analysis of Heterogeneous Aeromagnetic Data Reveals a Raw-Field Gradient-Reversal Anomaly at Uruana de Minas, Brazil”, Research Square, version 1, preprint, https://doi.org/10.21203/rs.3.rs-10707881/v1 [13]. An earlier version of the present study is available as Ribeiro LG and Simonssini MA (2026), “The Uruana de Minas Geomagnetic Gradient Anomaly: A Structurally Locked Reversal Envelope Persistent Across Four Decades”, Preprints.org, version 1, posted 15 September 2026, https://doi.org/10.20944/preprints202609.1201.v1 [37]. The Acta submission and the two preprint records are disclosed separately so that their respective questions, shared observations and publication status are explicit.

Conflicts of Interest

The authors declare no conflicts of interest.

Funding

Author Contribution

LGR: conceptualization, methodology, software, formal analysis, investigation, data curation, visualization, writing - original draft, and project administration. MAS: methodology, validation, formal analysis, investigation, and writing - review and editing. Both authors reviewed and approved the final manuscript and are accountable for the work.

Acknowledgement

The authors thank the Ágora Study Group, based in Uruana de Minas, Brazil, for discussion and intellectual exchange.

Data Availability

The study-generated derived datasets, result tables, frozen protocols, analysis and verification code, and archived verification outputs are supplied in Supplementary File S2. This includes the multiepoch structural analyses, the recovered scalar–triaxial audit and the exploratory addendum. Supplementary Files S1 and S3 provide the extended methods, results and figures. The data-access note in S2 identifies the source archives, access routes and file checksums.The original survey products are held by their public providers. SGB Projects 1009 (1971–1972; Convênio Brasil–Alemanha) and 3087 (2011; Formoso–Buritis–Lagoa Grande) are identified in the GeoSGB dataset catalogue at https://geosgb.sgb.gov.br/downloads/; the Project 3087 dataset page is https://geosgb.sgb.gov.br/downloads/index.php?dir=3087-Area19-Formoso_Buritis_Lagoa. Public consolidated products for ANP Project 0032 São Francisco (2008) are accessed through the São Francisco basin collection at https://reate.cprm.gov.br/arquivos/index.php/s/raz73BsTFYy9emP, linked from the official REATE portal at https://reate.cprm.gov.br/anp/TERRESTRE. The survey products used from these collections were obtained online.The individual scalar–triaxial file 0032_SAO-FRANCISCO_MED_PROC_00237.ASC was obtained directly from ANP/BDEP after an email request on 14 August 2026. ANP recovered it from IBM 3592 media and supplied it on 9 September 2026 under request 12638 and remittance bulletin 14498. Its delivery link was recipient-specific and time-limited; it is not a permanent public dataset URL. Requests for this file should be directed to data_download@anp.gov.br, identifying the survey and filename. S2 includes the remittance bulletin and

the matching file-identity record. Large upstream survey archives, including this original file, remain with their providers and are not redistributed in the supplement.

References

1. Beamish D, White JC. Aeromagnetic data in the UK: a study of the information content of baseline and modern surveys across Anglesey, North Wales. Geophys J Int. 2011;184:171–90. https://doi.org/10.1111/j.1365-246X.2010.04852.x.
2. Gavazzi B, Bertrand L, Munschy M, Mercier de Lépinay J, Diraison M, Géraud Y. On the use of aeromagnetism for geological interpretation: 1. Comparison of scalar and vector magnetometers for aeromagnetic surveys and an equivalent source interpolator for combining, gridding, and transforming fixed-altitude and draping data sets. J Geophys Res Solid Earth. 2020;125. https://doi.org/10.1029/2019JB018870. e2019JB018870.
3. Saltus RW, Chulliat A, Blakely RJ. Evaluation of aliasing in aeromagnetic surveys - update to Reid 1980 analysis. Earth Space Sci. 2026;13. https://doi.org/10.1029/2025EA004336. e2025EA004336.
4. Lahti I, Karinen T. Tilt derivative multiscale edges of magnetic data. Lead Edge. 2010;29:24–9. https://doi.org/10.1190/1.3284049.
5. Pilkington M, Tschirhart V. Practical considerations in the use of edge detectors for geologic mapping using magnetic data. Geophysics. 2017;82. https://doi.org/10.1190/geo2016-0364.1. J1-J8.
6. Guillard R, Gailler L, Labazuy P, Thebault E, Régis E, Dumont Q. Insight into magmatic pathways and subsurface structures from repeated UAV magnetic prospecting at Piton de la Fournaise volcano, Réunion Island. Earth Planet Space. 2025;77:169. https://doi.org/10.1186/s40623-025-02300-y.
7. Hokari T, Tanaka R, Hashimoto T, Koyama T. Shallow thermal activity of Tokachidake Volcano (Japan) investigated through repeated drone-borne magnetic surveys. Earth Planet Space. 2026;78:81. https://doi.org/10.1186/s40623-026-02417-8.
8. Ito R, Utsugi M. New magnetic inversion scheme including terrain-effect correction. Earth Planet Space. 2025;77:176. https://doi.org/10.1186/s40623-025-02276-9.
9. Phillips JD, Hansen RO, Blakely RJ. The use of curvature in potential-field interpretation. Explor Geophys. 2007;38:111–9. https://doi.org/10.1071/EG07014.
10. Sertcelik I, Kafadar O. Application of edge detection to potential field data using eigenvalue analysis of structure tensor. J Appl Geophys. 2012;84:86–94. https://doi.org/10.1016/j.jappgeo.2012.06.005.
11. Yuan Y, Huang D, Yu Q, Lu P. Edge detection of potential field data with improved structure tensor methods. J Appl Geophys. 2014;108:35–42. https://doi.org/10.1016/j.jappgeo.2014.06.013.
12. Yuan Y, Yu Q. Edge detection in potential-field gradient tensor data by use of improved horizontal analytical signal methods. Pure Appl Geophys. 2015;172:461–72. https://doi.org/10.1007/s00024-014-0880-1.

13. Ribeiro LG, Simonssini MA. (2026) Cross-Survey Analysis of Heterogeneous Aeromagnetic Data Reveals a Raw-Field Gradient-Reversal Anomaly at Uruana de Minas, Brazil. Research Square, version 1, preprint. https://doi.org/10.21203/rs.3.rs-10707881/v1
14. Pimentel MM, Rodrigues JB, DellaGiustina MES, Junges S, Matteini M, Armstrong R. The tectonic evolution of the Neoproterozoic Brasília Belt, central Brazil, based on SHRIMP and LA-ICPMS U-Pb sedimentary provenance data: a review. J S Am Earth Sci. 2011;31:345–57. https://doi.org/10.1016/j.jsames.2011.02.011.
15. Alkmim FF, Martins-Neto MA. Proterozoic first-order sedimentary sequences of the São Francisco craton, eastern Brazil. Mar Pet Geol. 2012;33:127–39. https://doi.org/10.1016/j.marpetgeo.2011.08.011.
16. Kuchenbecker M, Costa RD, Gomes DGC, Gouveia GV, Figueiredo RA, Pimenta JS. Projeto Fronteiras de Minas Gerais: Folha Buritis SD.23-Y-D-IV, escala 1:100,000. Relatório explicativo, mapa geológico e SIG. Belo Horizonte, Brazil: CODEMIG/UFMG; 2015.
17. Instituto Brasileiro de Geografia e Estatística (IBGE). (2025) Uruana de Minas: Cidades e Estados. https://www.ibge.gov.br/cidades-e-estados/mg/uruana-de-minas.html. Accessed 22 Aug 2026.
18. Estado de Minas Gerais. (1995) Lei nº 12.030, de 21 de dezembro de 1995. Assembleia Legislativa do Estado de Minas Gerais. https://www.almg.gov.br/legislacao-mineira/LEI/12030/1995/
19. Serviço Geológico do Brasil (SGB). (2026b) GeoSGB public aerogeophysical data: Project 1009 - Projeto Aerogeofísico Convênio Brasil-Alemanha. https://geosgb.sgb.gov.br/downloads/. Accessed 14 Aug 2026.
20. Agência Nacional do Petróleo. Gás Natural e Biocombustíveis (ANP) (2008) Acervo de dados técnicos não sísmicos: Projeto 0032 São Francisco. ANP, Brazil.
21. Serviço Geológico do Brasil (SGB). (2026a) GeoSGB public aerogeophysical data: Project 3087 - Area 19 - Formoso - Buritis - Lagoa Grande. https://geosgb.sgb.gov.br/downloads/. Accessed 14 Aug 2026.
22. Beggan CD, et al. International geomagnetic reference field: the fourteenth generation. Earth Planet Space. 2026;78:127. https://doi.org/10.1186/s40623-025-02360-0.
23. Gibson HA, Tailleur IL. (1980) Map showing relations between aeromagnetic data and geology, southern National Petroleum Reserve in Alaska. U.S. Geological Survey Open-File Report 80–516. https://doi.org/10.3133/ofr80516
24. Brown PJ. (2009) Aeromagnetic survey of Howard Pass quadrangle and the east half of Misheguk Mountain quadrangle, Alaska - a Web site for the distribution of data. U.S. Geological Survey Open-File Report 2009 – 1256. https://doi.org/10.3133/ofr20091256
25. Connard GG, Saltus RW, Hill PL, Carlson L, Milicevic B. (1999) Alaska digital aeromagnetic database description. U.S. Geological Survey Open-File Report 99–503. https://doi.org/10.3133/ofr99503
26. Johnson MR, Anderson ED, Ball LB, Drenth BJ, Grauch VJS, McCafferty AE, Scheirer DS, Schweitzer PN, Shah AK, Smith BD. (2019) Airborne Geophysical Survey Inventory of the Conterminous United

States, Alaska, Hawaii, and Puerto Rico (ver. 5.0, April 2024). U.S. Geological Survey data release. https://doi.org/10.5066/P9K8YTW1

27. Zanaga D et al. (2022) ESA WorldCover 10 m 2021 v200. https://doi.org/10.5281/zenodo.7254221
28. Agência Nacional de Energia Elétrica (ANEEL). (2026a) SIGEL geospatial transmission-line and substation services. https://sigel.aneel.gov.br/. Accessed 11 Sep 2026.
29. Agência Nacional de Energia Elétrica (ANEEL). (2026b) SIGA: Sistema de Informações de Geração da ANEEL. https://dadosabertos.aneel.gov.br/dataset/siga-sistema-de-informacoes-de-geracao-da-aneel. Accessed 11 Sep 2026.
30. Agência Nacional de Mineração (ANM). (2026) SIGMINE: Processos minerários ativos. https://geo.anm.gov.br/arcgis/rest/services/SIGMINE/dados_anm/MapServer/0. Accessed 11 Sep 2026.
31. OpenStreetMap contributors. (2026) OpenStreetMap data queried through the Overpass API. https://www.openstreetmap.org/. Accessed 11 Sep 2026.
32. Regan RD, Marsh BD. The Bangui Magnetic Anomaly: its geological origin. J Geophys Res Solid Earth. 1982;87:1107–20. https://doi.org/10.1029/JB087iB02p01107.
33. Taylor PT, Kis KI, Wittmann G. Satellite-altitude horizontal magnetic gradient anomalies used to define the Kursk Magnetic Anomaly. J Appl Geophys. 2014;109:133–9. https://doi.org/10.1016/j.jappgeo.2014.07.018.
34. Plado J, Kiik K, Jokinen J, Soesoo A. Magnetic anomaly of the Jõhvi iron ore, northeastern Estonia, controlled by subvertical remanent magnetization. Est J Earth Sci. 2020;69:189–99. https://doi.org/10.3176/earth.2020.13.
35. Korte M, Thébault E. Geomagnetic repeat station crustal biases and vectorial anomaly maps for Germany. Geophys J Int. 2007;170:81–92. https://doi.org/10.1111/j.1365-246X.2007.03387.x.
36. Freiman S, Granot R. AeroVmag: A new aero-towed vector magnetometer system. Geophysics. 2025;90. https://doi.org/10.1190/geo2024-0312.1. G139-G150.
37. Ribeiro LG, Simonssini MA. (2026) The Uruana de Minas Geomagnetic Gradient Anomaly: A Structurally Locked Reversal Envelope Persistent Across Four Decades. Preprints.org, version 1, preprint, posted 15 September 2026. https://doi.org/10.20944/preprints202609.1201.v1

Figures

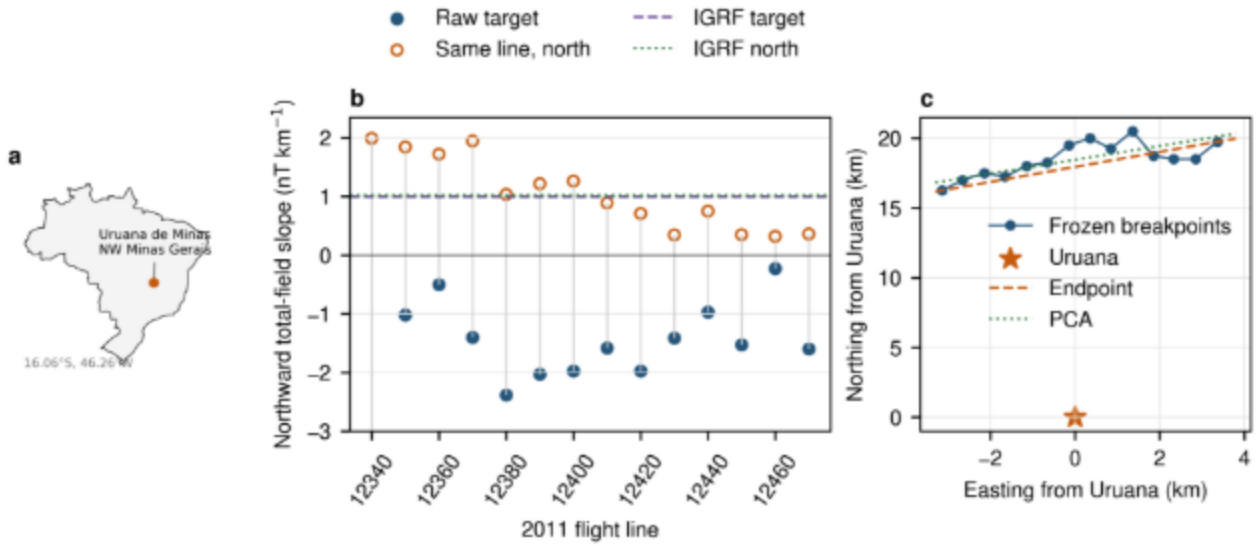

Figure 1

Geographic and self-contained 2011 baseline. (a) Brazil locator for Uruana de Minas; the point is the municipal-seat reference used only for geographic plotting. (b) Raw target slopes are negative on all 14 usable Project 3087 flight lines, whereas the same lines 16–20 km north are positive and IGRF medians remain positive in both zones. Median line-wise raw–IGRF residuals are −2.607 and +0.267 nT km−1; all 14 within-line control-minus-target residual contrasts are positive (median 2.922 nT km−1). The complete strict signature occurs at 6/97 regional centers. (c) Frozen negative-to-positive breakpoint chain with exact endpoint and PCA axial orientations. Country outline uses Natural Earth public-domain data; geographic coordinates are from IBGE (Source: the authors; country outline from Natural Earth and coordinates from IBGE)

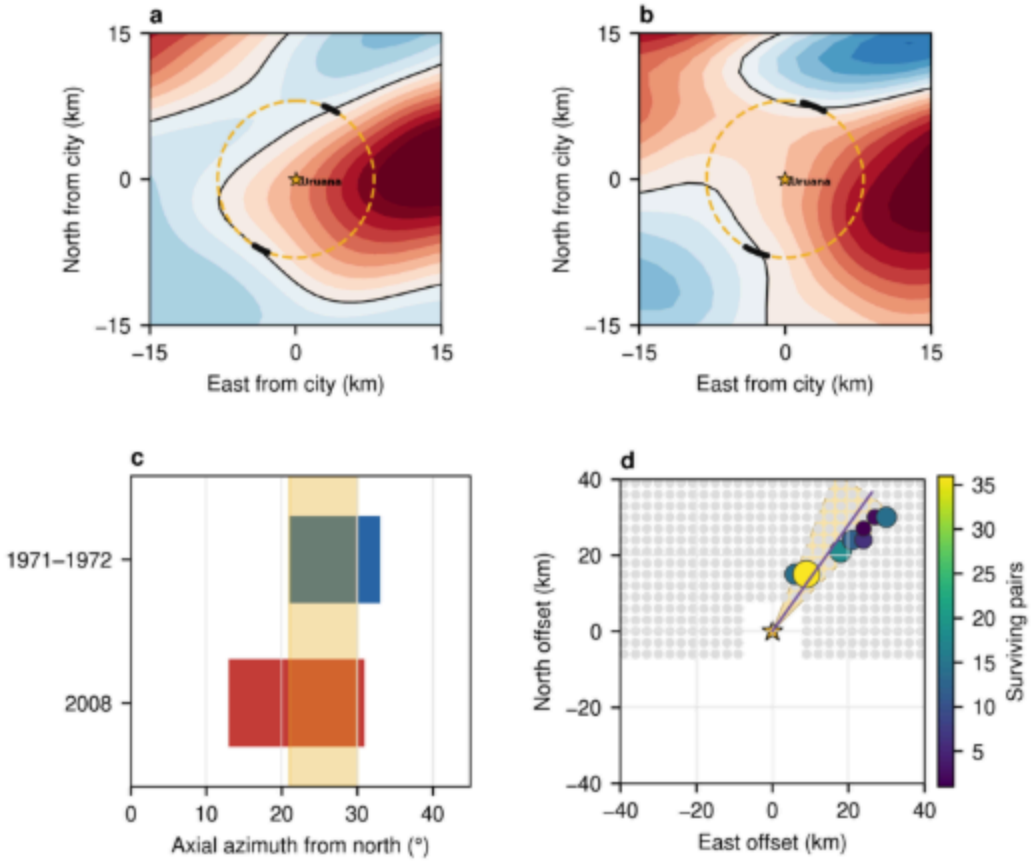

Figure 2

Persistent opposed magnetic-gradient walls around Uruana de Minas. (a,b) Canonical reconstructed 1971–1972 and corrected 2008 total-field dT/dN in the fixed annulus. Black segments mark antipodal axes; black contours mark dT/dN=0; the dashed circle marks the 8-km reference annulus. (c) The epochs share ten consecutive azimuths, 21–30° clockwise from north. (d) Only eight of 407 complete-support controls survive any matched specification pair, clustered in the shaded 23.199° sector containing 59/407 eligible centers (14.5%); point size and color show the number of pairings survived out of 108, and the purple line marks their survival-weighted direction; no control survives the strongest corrected-field pairings. The sector reference is post-discovery, does not preserve spatial dependence and is not an anomaly p-value. Full counts and the footprint reference are retained in S3 Section 4.3 and Fig. 2. Colors show derivative sign, not field intensity (Source: the authors)

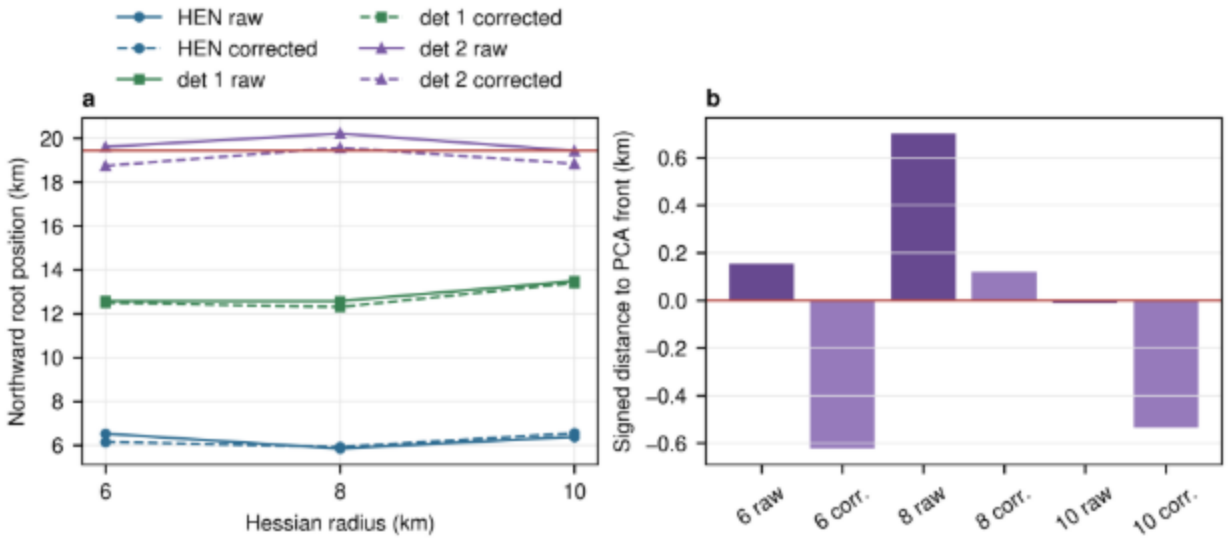

Figure 3

Nested 2008 curvature-phase roots and cross-epoch front registration. (a) Along the fixed +2 km E track, HEN=0 occurs near 6 km, the first det(H)=0 near 12–13 km and the second det(H)=0 near 19–20 km across radii and both 2008 channels. The horizontal reference is the intersection of the independently frozen 2011 PCA front with the same track. (b) Signed perpendicular distance from each outer 2008 root to the 2011 PCA line. All six lie within 0.702 km; the mean absolute separation is 0.358 km and their mean signed position is −0.032 km. This is cross-epoch geometric registration, not evidence of a concentric shell or source depth (Source: the authors)

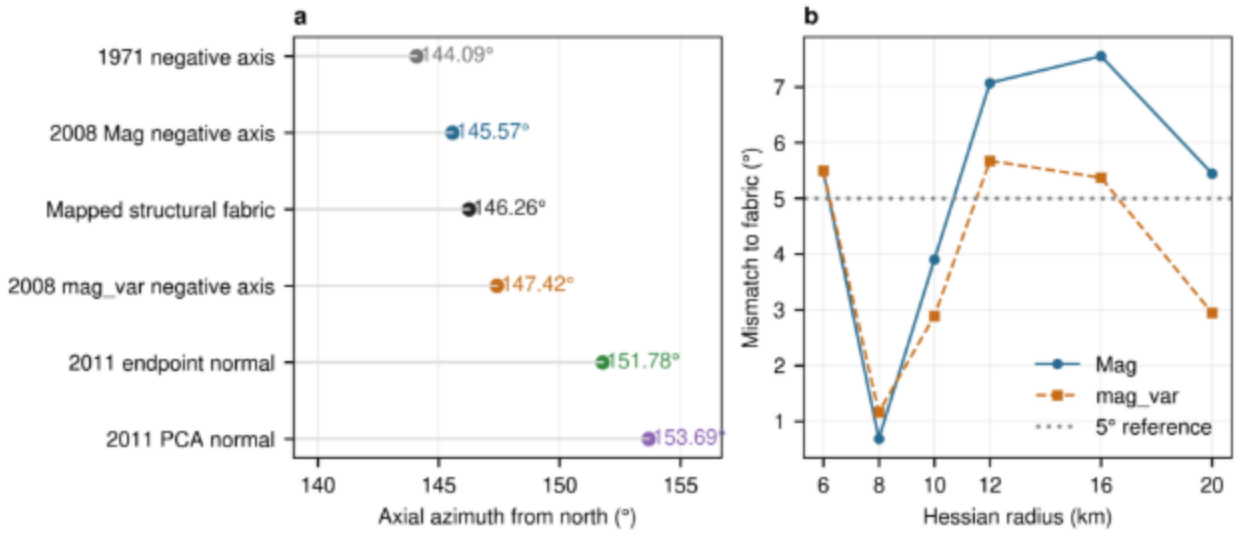

Figure 4

Structural locking across independent orientation domains. (a) Historical 1971 and 2008 negative-curvature axes, mapped structural fabric, and normals to the exact 2011 breakpoint front occupy the same narrow axial family. (b) Mismatch between the fixed structural axis and the 2008 negative-curvature axes across 6–20 km Hessian radii (Source: the authors)

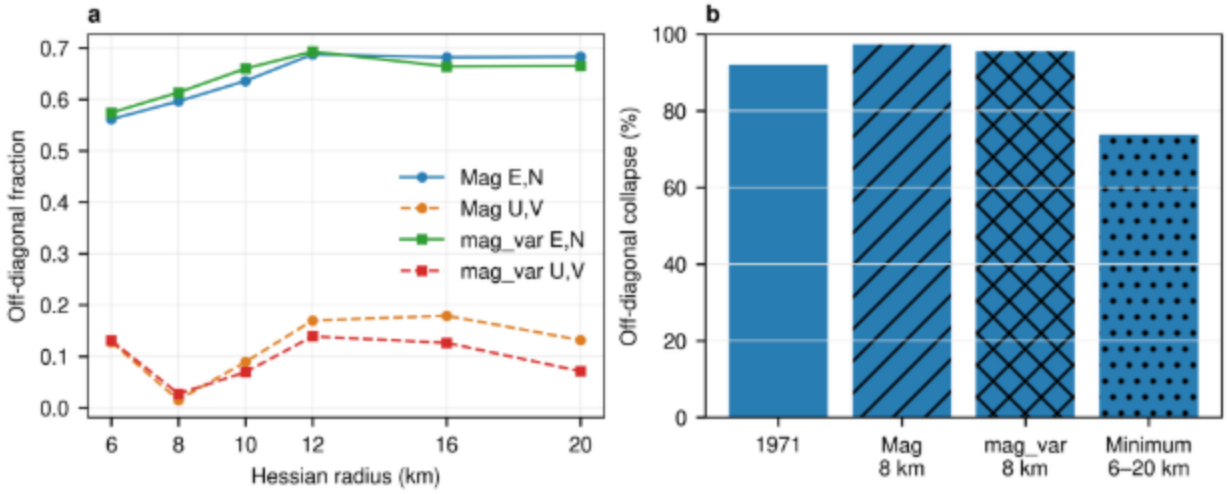

Figure 5

Structural-frame diagonalization. (a) Geographic E,N versus structural U,V off-diagonal Hessian fractions across the 2008 scale ladder. (b) Collapse of the off-diagonal term in the 1971 historical Hessian, 2008 8-km raw/corrected Hessians and the conservative multiscale 2008 minimum (Source: the authors)

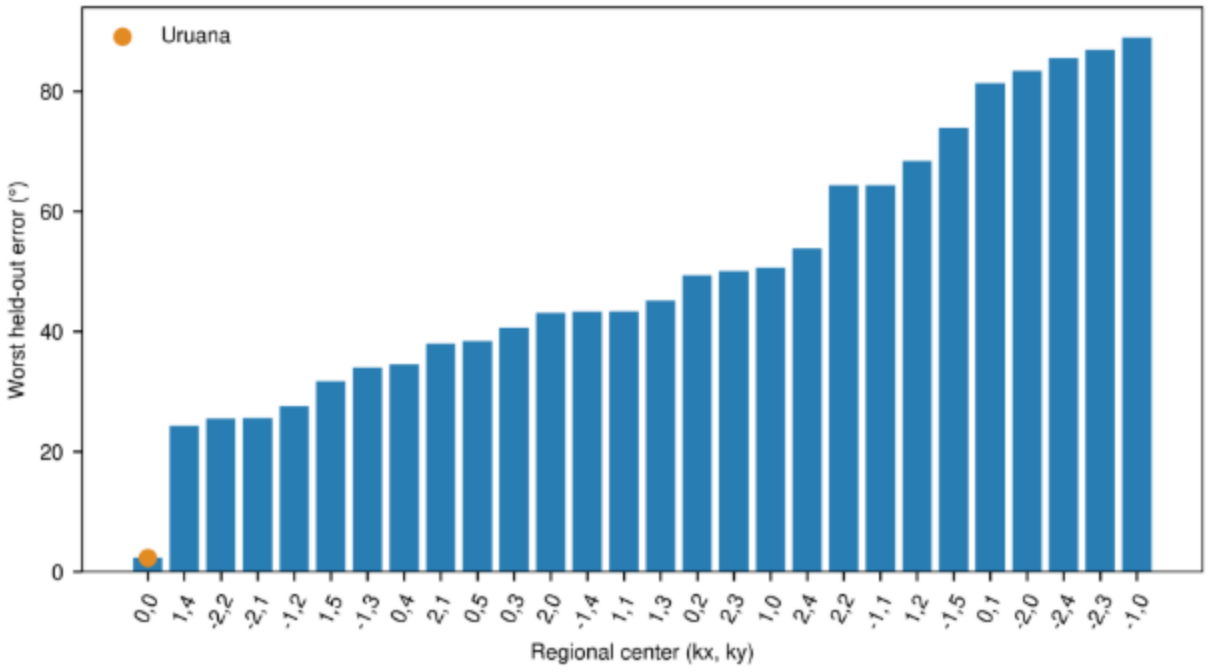

Figure 6

Three-domain leave-one-out reconstruction. At each regional center, two of three independent orientation domains - historical 1971 Hessian, 2008 Hessian, and mapped structural grain - reconstruct the third by axial circular mean. Uruana has the smallest worst held-out error (2.287 deg) among 28 centers; the next center is 24.263 deg (Source: the authors)

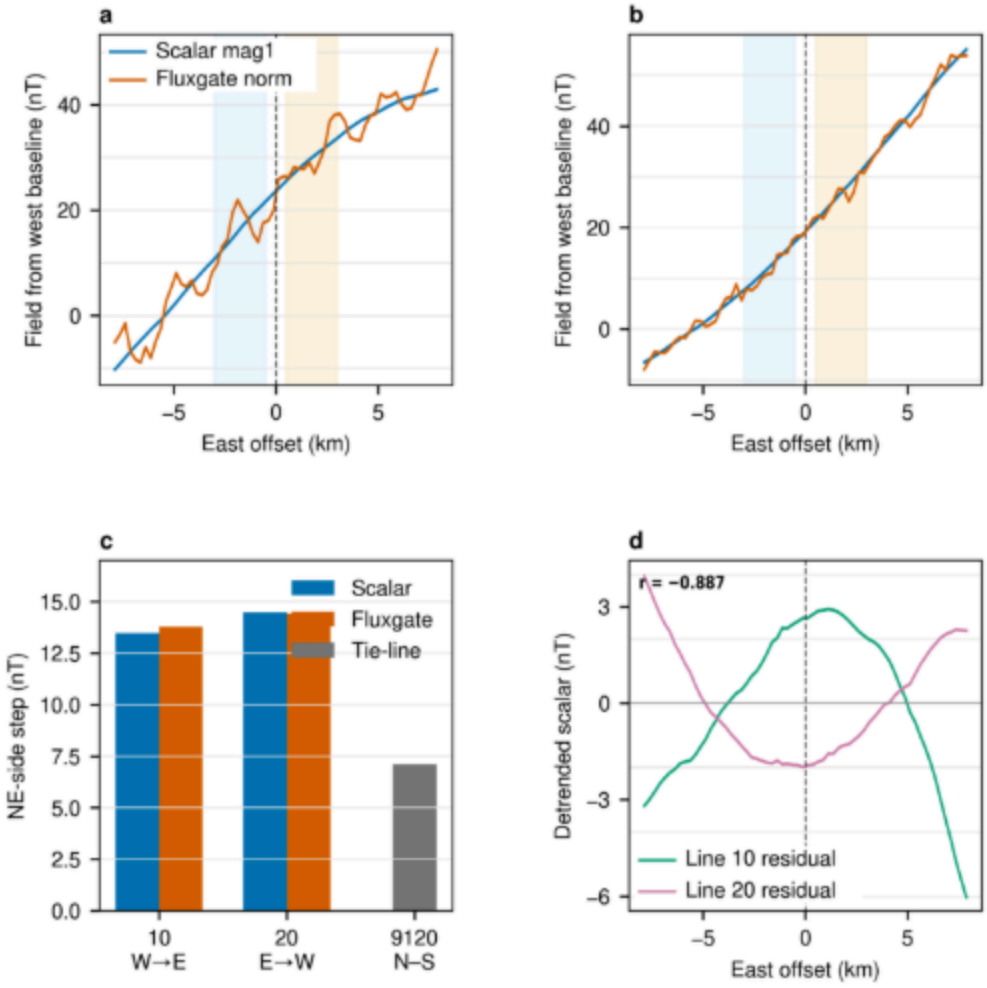

Figure 7

Reciprocal-flight, dual-sensor audit of the recovered original 2008 file. (a,b) Production lines 10 (west to east) and 20 (east to west), respectively: scalar mag1 and rotation-invariant fluxgate-norm profiles at two fixed São Domingos crossings traversed in opposite flight directions; shading marks the side windows. (c) Both sensors retain the same fault-side increase on the reciprocal lines, while orthogonal tie-line 9120 independently reproduces that side-of-fault direction 63 days earlier. (d) Linear-background residuals do not reproduce the same local waveform. This failure distinguishes a stable boundary from a repeated compact-body fingerprint (Source: the authors)

Supplementary Files

This is a list of supplementary files associated with this preprint. Click to download.

- 04SupplementaryMaterialS1S2S3.zip